

See discussions, stats, and author profiles for this publication at: <https://www.researchgate.net/publication/262817161>

Flexible High-Energy Li-Ion Batteries with Fast-Charging Capability

ARTICLE *in* NANO LETTERS · JUNE 2014

Impact Factor: 13.59 · DOI: 10.1021/nl501597s · Source: PubMed

CITATIONS

20

READS

136

11 AUTHORS, INCLUDING:



[Sanghan Lee](#)

Stanford University

14 PUBLICATIONS 470 CITATIONS

[SEE PROFILE](#)



[Sinho Choi](#)

Ulsan National Institute of Science and Techn...

25 PUBLICATIONS 144 CITATIONS

[SEE PROFILE](#)



[Hyejung Kim](#)

Ulsan National Institute of Science and Techn...

8 PUBLICATIONS 663 CITATIONS

[SEE PROFILE](#)



[Soojin Park](#)

Ulsan National Institute of Science and Techn...

152 PUBLICATIONS 4,193 CITATIONS

[SEE PROFILE](#)

Flexible High-Energy Li-Ion Batteries with Fast-Charging Capability

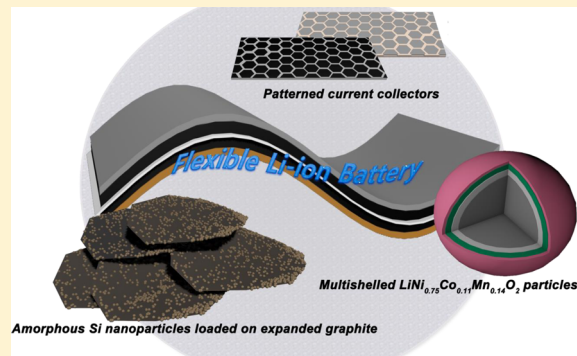
Mi-Hee Park,[†] Mijung Noh,[†] Sanghan Lee, Minseong Ko, Sujong Chae, Soojin Sim, Sinho Choi, Hyejung Kim, Haisol Nam, Soojin Park,* and Jaephil Cho*

[†]School of Energy and Chemical Engineering, Ulsan National Institute of Science and Technology (UNIST), 689-798, Ulsan, South Korea

Supporting Information

ABSTRACT: With the development of flexible mobile devices, flexible Li-ion batteries have naturally received much attention. Previously, all reported flexible components have had shortcomings related to power and energy performance. In this research, in order to overcome these problems while maintaining the flexibility, honeycomb-patterned Cu and Al materials were used as current collectors to achieve maximum adhesion in the electrodes. In addition, to increase the energy and power multishelled $\text{LiNi}_{0.75}\text{Co}_{0.11}\text{Mn}_{0.14}\text{O}_2$ particles consisting of nanoscale V_2O_5 and $\text{Li}_x\text{V}_2\text{O}_5$ coating layers and a $\text{Li}_{\delta}\text{Ni}_{0.75-z}\text{Co}_{0.11}\text{Mn}_{0.14}\text{V}_z\text{O}_2$ doping layer were used as the cathode–anode composite (denoted as PNG-AES) consisting of amorphous Si nanoparticles (<20 nm) loaded on expanded graphite (10 wt %) and natural graphite (85 wt %). Li-ion cells with these three elements (cathode, anode, and current collector) exhibited excellent power and energy performance along with stable cycling stability up to 200 cycles in an *in situ* bending test.

KEYWORDS: Flexible Li-ion battery, fast charging, volume expansion, *in situ* bending, cation mixing



Recently, flexible Li-ion batteries have become important for portable electronics applications such as wearable devices or roll-up displays.^{1–4} These types of rechargeable batteries require fast charging rather than fast discharging, because consumers want to charge the portable electronics faster than ever. In addition, these batteries should have long guaranteed cycle lifetimes even after hundreds of repetitive bending and stretching deformations. Flexible primary batteries have been developed for similar applications, but they cannot be used in mobile electronics because they are impossible to recharge.⁵ From a practical viewpoint, flexible batteries must have (1) high electrode capacities, (2) mechanical flexibility, and (3) the cathode or anode materials should have higher capacities than the currently dominant LiCoO_2 , $\text{LiNi}_{0.6}\text{Co}_{0.2}\text{Mn}_{0.2}$, and graphite.

The reports on electrode materials of flexible batteries so far have mostly been focused on anodes, and CNT, graphene, carbon nanofibers, and metal oxides have been intensively investigated.^{2,6–8} In particular, carbon-based materials have been widely used with metal-based anodes because of their high chemical stability, easy manipulation into various flexible morphologies due to high mechanical stability, and high conductivity.^{9–11} Flexible batteries composed of these active materials have exhibited fast discharging rate capabilities because of their thin-film nature. For instance, flexible batteries consisting of graphene foam with LiFePO_4 and $\text{Li}_4\text{Ti}_5\text{O}_{12}$ active materials showed 76% capacity retention at a 185 °C discharging rate owing to the 3D nature of the graphene foam.¹²

Considering the working voltage and electrode density, natural graphite has a high electrode density of $\sim 1.5 \text{ g cc}^{-1}$, a low discharge profile, and a low electrode thickness expansion ratio (<30%). This makes it the best candidate for flexible batteries, but its relatively low utilized capacity of <360 mAh g^{-1} remains a problem. As for Si anodes, although they have large capacities of >3000 mAh g^{-1} , they exhibit unacceptable volume expansion ratio of >300% after only a couple of cycles and a low electrical conductivity impedes their utilization of the fast-charging flexible batteries.^{13,14}

On the cathode side, LiCoO_2 may be the dominant material used currently, but its relatively low capacity compared to those of Ni-based cathodes impedes its usage in practical battery applications.¹⁵ Alternatively, flexible cathodes consisting of networks of flexible CNTs and nanosized LiMn_2O_4 powders have been reported but the inherent drawbacks of LiMn_2O_4 , such as its low volumetric capacity and high rate capability, were not resolved.¹⁶ Alternatively, Ni-based cathode materials, for example, $\text{LiNi}_{0.6}\text{Co}_{0.2}\text{Mn}_{0.2}\text{O}_2$, are possible candidates for achieving high density and high capacity, but high contents of surface impurities (e.g., Li_2CO_3 , LiOH , and water) that are naturally formed as a uniform layer and a high pH of powder critically increase the cathode resistances at higher current rates and increase the prevalence slurry gelation.^{17–20} To address

Received: April 30, 2014

Revised: May 26, 2014

Published: June 3, 2014



these problems, coating the materials, such as Al_2O_3 , ZrO_2 , AlPO_4 , and AlF_3 at $>500^\circ\text{C}$ or washing the pristine cathodes have been proposed,²¹ but these coating or washing procedures did not cause drastic decreases in the amount of impurities or in the pH. Furthermore, the metal oxide coating layers act as insulators at higher current rates that impede fast charge transfer at the interface.²²

Another important technical hurdle for fabricating flexible battery is to develop an appropriate current collector. Nonpatterned Al and Cu current collectors have poor adhesion with the electrode because of the limited contact area, resulting in fatal peeling-off of the electrodes during bending or folding.²³ To solve this problem, surface modification of the current collectors using direct chemical vapor deposition (CVD) processes or increasing its contact area using nanostructured Si or $\text{Li}_4\text{Ti}_5\text{O}_{12}$ or Fe_2O_3 anodes with nanorod, nanowire, and nanoporous morphologies have been reported.^{24,25} However, these approaches did not actually prevent the peeling-off problem after hundreds cycles of continuous bending and stretching.

To realize flexible, high-energy full cell with fast charging capability and stable cycling performance even under *in situ* bending and stretching over 200 cycles, we considered the three main components of the cell: the current collector, cathode, and anode. First, honeycomb-patterned Al and Cu current collectors were prepared by reactive-ion etching (RIE) process (Supporting Information Figure S1). Well-patterned Al and Cu foils with a pattern width of $50\ \mu\text{m}$ (Figure 1a,b) and depths of

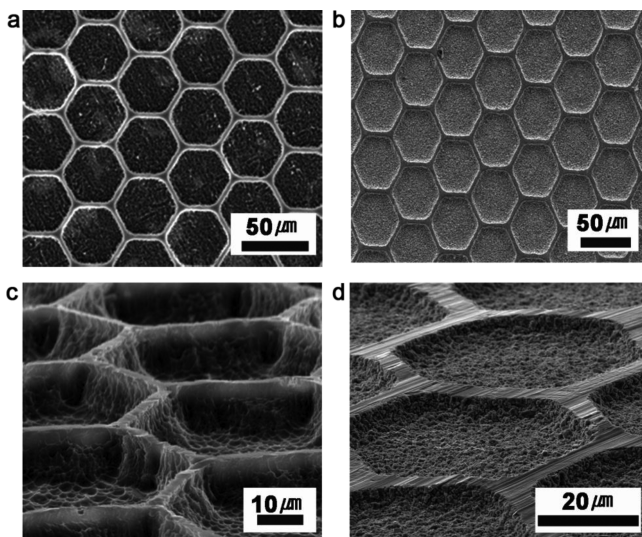


Figure 1. (a,b) Scanning electron microscopy (SEM) images (top view) of patterned Al and Cu foil. (c,d) SEM images (tilted view) of patterned Al and Cu foil.

10 and $5\ \mu\text{m}$, respectively (Figure 1c,d), were obtained. In the patterns of $<1\ \mu\text{m}$ on rough surface by etching process, surface area enhancement (compared to nonpattern and pattern with tens-of-micrometer dimension) is remarkably increased. When we take into account the pure current collector, decreasing pattern dimension (to nanometer scale) increases flexibility and mechanical strength of the current collector. However, dimension of active materials is also an important factor to affect adhesion between active material and patterned current collector. When the particle size of active materials is exactly matched with patterned current collector, we cannot expect a

strong adhesion of active materials to the current collector. That is why we used tens-of-micrometer-sized honeycomb patterns in this study. Actually, this pattern has microscale and nanoscale patterns that formed during a standard photolithographic process. The combination of micro- and nanoscale patterns significantly increases the mechanical strength of the current collector and adhesion of active materials to the current collector. We confirmed the characteristics of the patterned Al (or Cu) current collectors by noncontact mode phase-shifting interferometry, which yields a three-dimensional (3D) stereogram that can be analyzed to characterize the morphology, roughness, and depth over a surface of large area (Supporting Information Figure S2b). On the basis of our estimate, the surface area was ~ 1.7 times higher for the honeycomb-patterned foil than for the nonpatterned one. The active materials that are strongly anchored to the patterned Cu substrates are supposed to provide a significantly reduced crack after bending. In addition, a pattern direction for bending plays an important role in determining strong adhesion between current collector and active material. Supporting Information Figure S4a,c shows vertical bending test of the trench-type patterned Cu substrate to the pattern direction. Many cracks are formed in the electrodes. In contrast, parallel bending test to the pattern direction significantly decrease cracks after bending test (Supporting Information Figure S4b,d). These results suggest that the patterning direction and bending direction can affect the adhesion of active materials to the patterned current collector, because mechanical stress in terms of bending direction is different depending on patterned direction. According to pattern shapes of current collectors, bending direction and pattern direction should be considered. That is why we choose honeycomb-type pattern in this study. In this pattern, mechanical stress in terms of bending direction is the same everywhere. Thus, there should be a larger contact area between the electrode and the collector and therefore significantly enhanced adhesion (Supporting Information Figure S3). We believe that this enhancement may prevent the delamination of the composite electrode from the collector, resulting in stable electrochemical performance during rolling and bending tests.

As for the cathodes, we aimed to maximize the utilization of Ni-based cathodes' electrochemical performance by adopting a layered $\text{LiNi}_{0.75}\text{Co}_{0.11}\text{Mn}_{0.14}\text{O}_2$ material. The X-ray diffraction (XRD) patterns of the pristine $\text{LiNi}_{0.75}\text{Co}_{0.11}\text{Mn}_{0.14}\text{O}_2$ (BNCM) and the multishelled $\text{LiNi}_{0.75}\text{Co}_{0.11}\text{Mn}_{0.14}\text{O}_2$ (VNCM) powders indicated a well-defined layered structure with space group $R\bar{3}m$ without impurity peaks (Supporting Information Figure S5). The surface morphology of pristine BNCM consisted of roundshaped secondary particles of approximately $10\ \mu\text{m}$ in size that were aggregated with micrometer-sized primary particles, and its tap density was $2.6\ \text{g cc}^{-1}$ (Supporting Information Figure S6). Further, to achieve high electrode density of $1.5\ \text{mAh/cm}^2$ (about $3.2\ \text{g/cm}^3$), the micrometer-sized particles should be used as a cathode; this is why we could not use bulky nanoparticles.

However, the water content of the as-synthesized BNCM sample was 700 ppm. For the cathode powder, reducing the amount of residual LiOH , H_2O , and Li_2CO_3 impurities is very important, because such impurities impede the Li^+ diffusivity and charge transfer reactions at the interface and accelerate the formation of HF. Furthermore, Li_2CO_3 has been reported to be a main source of CO_2 gas at 60°C . In addition, the pH of the cathode powder in water should be below 12, otherwise the

cathode composite slurry in *N*-methyl-2-pyrrolidone (NMP) solvent exhibits a rapid increase in viscosity and ultimately gelation.²⁶ To overcome these problems, NH₃VO₃ was used as a coating precursor, because ionized VO₃⁻ bonds with Li⁺ ions from LiOH and Li₂CO₃ on the particle surface (Supporting Information Figure S7). This coating method results in a uniform coating on the final product after annealing at 400 °C for 3 h. After the coating process, the surface of the pristine sample appears to be uniformly covered with nanoparticles (Supporting Information Figure S6d).

The transmission electron microscopy (TEM) image of a VNCM sample cross-sectioned using an FIB (focused-ion-beam) shows that the cathode particle surface is covered with an amorphous layer that is ~8–10 nm thick (Figure 2a).

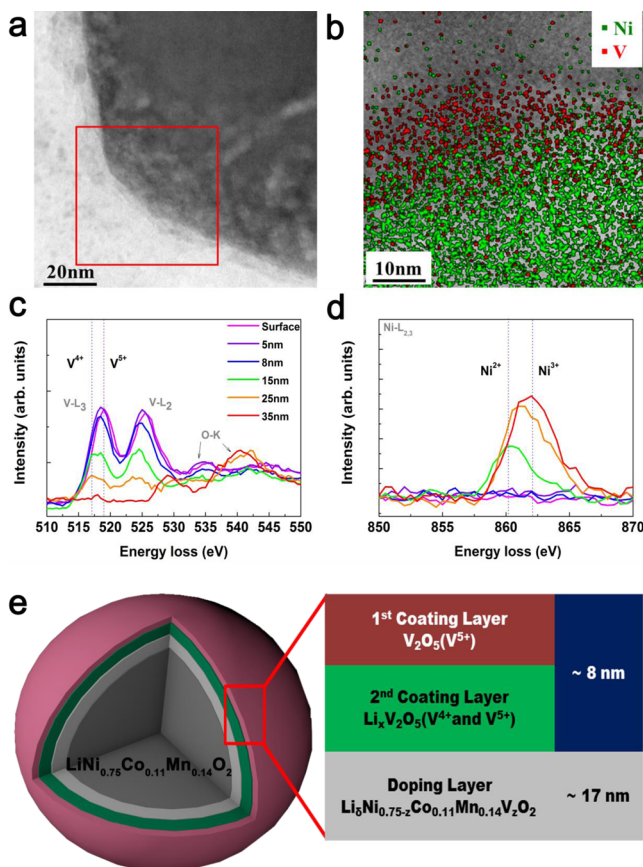


Figure 2. (a) Cross-sectional TEM image of the VNCM. (b) EDX mapping of Ni (green) and V (red) in (a). (c, d) EELS spectra of V and Ni along the arrow direction in (b) to a depth of ~35 nm. (e) Schematic of the composition of the cathode material.

Energy dispersive X-ray (EDX) mapping of the Ni and V elements in the red rectangular area showed that the V is confined to the surface area (Figure 2b). Furthermore, the line scanning along the yellow arrow again shows that V is only observed up to ~8–10 nm deep from the surface after which Ni and V coexist to a depth of ~25 nm. Finally, deeper than ~25 nm, only Ni is observed (Supporting Information Figure S8). This result agrees with the electron energy loss spectra (EELS), which show both V and Ni in the region ~25 nm deep from the surface (Figure 2c,d) but dominantly V⁵⁺ in the outmost layer. However, the V oxidation state decreases to V⁴⁺ deeper in the sample (see the spectra at ~8 nm), showing that the surface coating layer consists of V₂O₅ and Li_xV₂O₅ layers,

where the Li_xV₂O₅ layer forms from the reaction with residual Li impurities on the surface or Li in the bulk phase. Simultaneously, the presence of Ni²⁺ at depth of ~15 nm indicates the oxidation state of Ni³⁺ to Ni²⁺ to balance the oxidation state of V⁴⁺. At a depth of ~25 nm, the Ni peak was shifted to the right, showing the formation of Ni³⁺. This shift is concomitant with the disappearance of V peak, meaning that V was confined to within ~25 nm of the surface. Overall, as shown in Figure 2d, the surface of the cathode consists of several layers within ~25 nm of the surface: amorphous V₂O₅, Li_xV₂O₅, and Li_{0.75-z}Co_{0.11}Mn_{0.14}V₂O₂. Deeper than ~25 nm, the particles are composed of LiNi_{0.75}Co_{0.11}Mn_{0.14}O₂ only. Note that VNCM shows a decreased powder pH of 11.85, compared to the pH of 12.20 in BNCM (Supporting Information Figure S9). As described in the introduction, the main problem of high N-rich cathode materials is high amounts of residual lithium impurities, such as LiOH and Li₂CO₃, act as insulators, which deteriorate the electrochemical performances and also increases powder pH, once ammonium metavanadate was coated and followed by annealing at 400 °C. Those impurities were reacted with ammonium metavanadate, thus forming multishelled layers including Li_xV₂O₅ (see Supporting Information Figure S7). Accordingly, Li_xV₂O₅ decreases the powder pH (see Supporting Information Figure S9) and also expects to enhance the rate capability of the cathode.

The X-ray photoelectron spectroscopy (XPS) profile for C 1s in the samples showed that the carbon peak from Li₂CO₃ almost disappeared after coating (Supporting Information Figure S10). Despite the importance of these aspects of the layer Ni-based cathodes for commercial systems, recent studies have mostly ignored this topic.^{27,28} In consequence, such multishelled layers in VNCM cathode led to significantly decreased disordered cation mixing layers^{29–31} (Supporting Information Figure S11). In terms of electrochemical performance, when the transition metal ions reside in the lithium sites due to cation mixing, they impede Li⁺ diffusivity.

It has been reported that the limiting factor for Li⁺ diffusivity is surface diffusion rather than bulk diffusion, and facilitating Li⁺ transport across the surface by creating an amorphous layer with high Li⁺ mobility is the most feasible way to improve the rate capability.³² The higher electrical conductivity for the amorphous V₂O₅ nanoparticles (1.85×10^{-4} S cm⁻²)³³ than for Ni-based cathodes (e.g., LiNi_{0.7}Co_{0.15}Mn_{0.15}O₂; 9.3×10^{-6} S cm⁻²)²⁸ also facilitates faster charge transfer at the interface. Actually, the Li⁺ diffusivity estimated from Warburg impedance in the VNCM is ~2 orders of magnitude higher values than in the BNCM at 24 °C at a 0.1 C charging rate (Supporting Information Figure S12).

The first charge and discharge curves of VNCM electrode exhibit a relatively high discharge capacity of 211 mAh g⁻¹ with a Coulombic efficiency of 90.5% between 3.0 and 4.5 V at 0.1 C rate (= 21 mA g⁻¹) at 24 °C (Figure 3a). In contrast, BNCM showed a slightly lower capacity of 207 mAh g⁻¹ with a Coulombic efficiency of 88.5%. The loading levels of both BNCM and VNCM in the electrodes were 7 mg cm⁻² (3.2 g cc⁻¹). The decrease in the initial irreversible capacity of the VNCM is believed to be due to the decreased amount of LiOH and Li₂CO₃ impurities. Fast charging capability is of paramount importance for fast-charging flexible batteries. The voltage profile of the VNCM shows a lower IR drop than that of the BNCM above 3 C rate during the charge cycle, which leads to a higher rate capability (Supporting Information Figure S13). It is speculated that VNCM has a lower charge-transfer resistance,

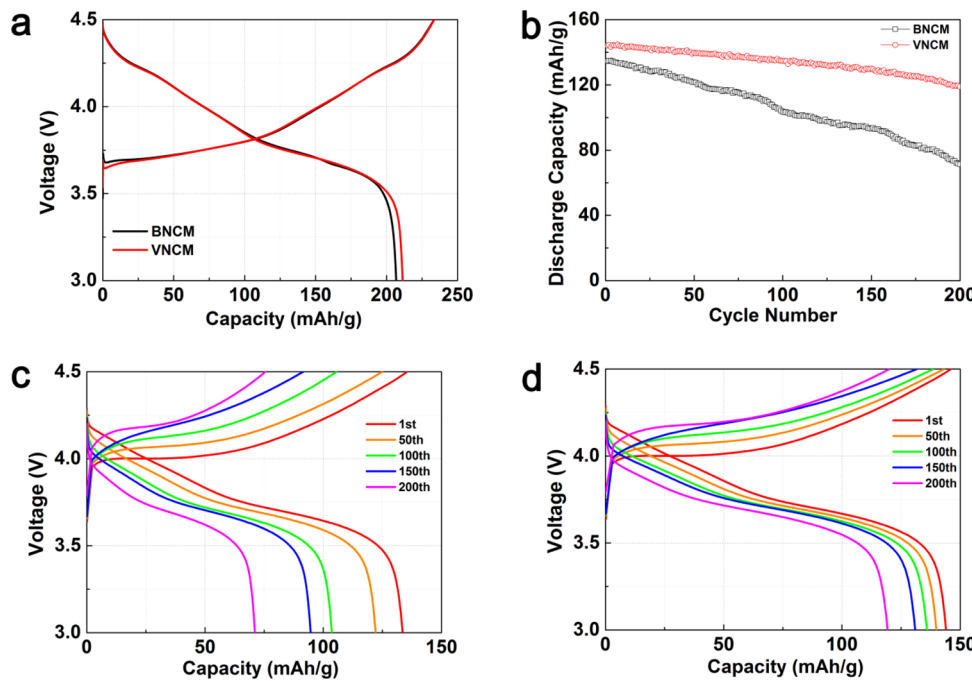


Figure 3. (a) First charge–discharge curves of BNCM and VNCM at 0.1 C rate. (b) Continuous cycling results for BNCM and VNCM at a 5 C charging rate at 24 °C (discharge rate was fixed at 0.5 C). Charge and discharge profiles of (c) BNCM and (d) VNCM after the 1st, 50th, 100th, 150th, and 200th cycles.

which facilitates faster Li^+ intercalation/deintercalation reactions at the surface layer between the cathode and the electrolyte. In order to confirm the fast charge rate capability of this electrode, a 5 C rate ($= 1050 \text{ mA g}^{-1}$) charging test was carried out using both samples for a discharge rate fixed at 0.5 C (Figure 3b). The first charge capacity of the VNCM (144 mAh g^{-1}) is much higher than that of the BNCM, and the capacity retention gap between the two electrodes after 200 cycles is even more pronounced; the capacity retention is 83 and 56% for the VNCM and BNCM, respectively. It should be noted that the lower amounts of lithium impurities on the VNCM surface due to the coating layers also lead to improved rate capability.

Finally, for the anode minimizing the volume expansion is of critical importance, otherwise the electrode will peel-off from the current collector during bending and stretching despite the use of patterned collectors. In addition, it is essential to use amorphous Si that has a lower activation energy barrier and reduced structural strain during lithiation/delithiation.³⁴ In order to control the Si particle size and crystallinity, we simply decomposed SiH_4 gas at 550 °C for 30 min to easily obtain amorphous Si nanoparticles with an average particle size of 20 nm. In addition, the high surface area of flake-type expanded graphite, which has a high electrical conductivity, leads to easy uniform deposition of the Si nanoparticles.

In order to achieve a high density of the anode, comparable to the density of 1.5 g cc^{-1} for natural graphite, a composite consisting of 5 wt % binder, 85 wt % potato-shaped natural graphite, and 10 wt % amorphous Si nanoparticle-loaded expanded graphite (denoted as PNG-AES) was used (Supporting Information Figure S14–18). The loading level of the active material in the composite electrode was 5.3 mg cm^{-2} ($>1.5 \text{ g cc}^{-1}$). The first charge (lithium intercalation) and discharge capacities of the PNG-AES sample are 670 and 569 mAh g^{-1} , respectively, which correspond to 85% Coulombic

efficiency, and it shows a capacity retention of 98.5% after 100 cycles at a 0.5 C rate (Supporting Information Figure S18c). More importantly, after 100 cycles the electrode thickness increased to $57 \mu\text{m}$ from $44 \mu\text{m}$ (Supporting Information Figure S18g,h). This is a volume expansion ratio of $\sim 30\%$, which is quite comparable to that of natural graphite. This ratio was also confirmed by measuring the thickness using a micrometer.

From the patterned foils, a multishelled VNCM cathode and a PNG-AES anode, pouch-type Li-ion cells with a nominal capacity of 15.6 mAh (6 cm (length) $\times 2 \text{ cm}$ (width)), were fabricated in a dry room. Here, loading level of the active cathode is 7 mg cm^{-2} , and this is the first ever report of fast charging at such a high loading. Figure 4a shows the charging rate capability of the pouch-type full cell with the VNCM cathode and PNG-AES anode between 3.0 and 4.3 V at charging rates of 0.1, 0.6, 2, 4, 7, 12, and 20 C, where the discharge rate was fixed at 0.5 C ($1 \text{ C} = 15.6 \text{ mAh}$). The cell delivers excellent charge capacities of 185, 169, 161, 146, 131, 117, and 91 mAh g^{-1} at these rates, respectively. In addition, the capacity retention of the cell in charging tests at 4 C and at 12 C rates was 63% after 350 cycles and 50% after 600 cycles (Figure 4c,e). Such capacity retention under rapid charging conditions has not been reported previously. A Ragone plot of the specific energy and power of the cathode electrode for comparison of its charging rate performance is shown in Figure 4f. At low power (0.1 C, $82 \text{ W kg}_{\text{electrode}}^{-1}$), the gravimetric energy of the VNCM/PNG-AES electrode was $733 \text{ Wh kg}_{\text{electrode}}^{-1}$, which is higher than that of BNCM (Supporting Information Figure S19,20). More importantly, the specific energy density was maintained at $368 \text{ Wh kg}_{\text{electrode}}^{-1}$ at a specific power of $8200 \text{ W kg}_{\text{electrode}}^{-1}$ when the cell was charged for 3 min. This result demonstrates the higher specific energy density of this electrode at high rates.

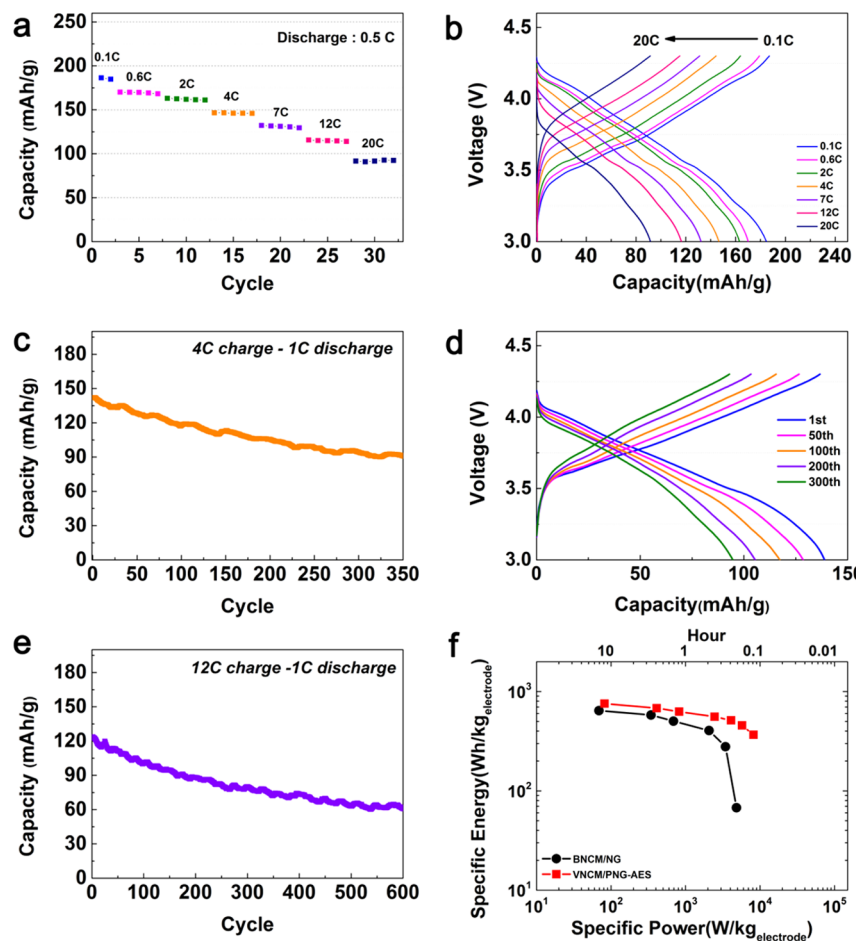


Figure 4. (a) Galvanostatic charge–discharge curves of the full cell at 0.1 C rate at 24 °C. (b,c) Cycling performance of the cell for charging at 4 and 12 C rates and discharging at 1 C rate. (c) Charging rate capability of the cell with increasing charging rates from 0.1 to 20 C (discharging rate was fixed at 0.5 C). (d) Corresponding voltage profiles for (c). (e) Cycling performance at 12 C rate. (f) Ragone plot representing the charging rate performance, calculated from the galvanostatic data in Figure 5a,b. The width and length of the cell were 2 and 6 cm, respectively, and the cell capacity was 15.6 mAh. Only the cathode electrode weight was considered in the gravimetric energy and power density calculations.

Because flexibility of the Li-ion cells is very important for flexible electronic devices, an in situ bending test was carried out at speed of 30 mm min⁻¹ with a simultaneously applied torque of 11 N. Ten bending and stretching cycles were carried out on the cell per electrochemical cycle. Figure 5a shows photographs of the pouch-type full cell before and after bending (Supporting Information Video 1). This cell was cycled under continuous bending and stretching at 4 C rate for both charge and discharge over 200 cycles between 4.3 and 3.0 V (Figure 5b). After 200 cycles, its capacity retention was only 23% lower than that of a control sample not subjected to bending (Figure 4c). Supporting Information Figure S21 displays images of the cathode and anode electrode separated from the full cell after 100 electrochemical cycles with in situ bending. The electrode materials were not separated from the patterned current collectors, while separation had occurred for the nonpatterned ones. Moreover, the change in the open-circuit voltage of the full cell at 3.9 V was tested over 10 days under in situ conditions (Figure 5c), and its drop after 10 days was found to be only 0.08 V. This result is far superior to that of previous cable-type Li-ion battery.^{1,2} These results are attributed to the strong adhesion between the composite electrode materials and the patterned current collectors.

We have developed the flexible batteries with fast charging capability by using high-power cathode and anode materials

and honeycomb patterned current collector. A multishelled VNCM cathode material consisting of amorphous V₂O₅ and Li_xV₂O₅ coating layers and Li_δNi_{0.75-x}Co_{0.11}Mn_{0.14}V₂O₂ coating layers resulted in a significantly improved fast charge capability of the cathode. Further such multishell layers prevented any side reactions with the electrolytes and moisture in the air also provided such excellent rate capability. Nature of amorphous Si nanoparticles with <20 nm in size and highly conductive EG backbone enabled to both accommodate the volume changes and fast Li ion movement. Also, we used honeycomb-patterned Al and Cu substrates to obtain strong adhesion with the electrode under severe bending and stretching conditions. Surprisingly, the flexible Li-ion battery adopting the new anode, cathode, and patterned substrates exhibited exceptional cycling performance over 600 cycles even at 12 C rate cycling. In addition, a fast charging time of 3 min (= 20 C rate) was possible with 50% capacity retention. More importantly, the in situ bending test over 200 electrochemical cycles at 4 C rate showed very stable cycling behavior. Further, we believe that our flexible battery is worthy of attention as the first attempt which means fast charge and high energy density of commercial levels.

Experimental Methods. Synthesis of VNCM. In order to prepare the Ni_{0.75}Co_{0.11}Mn_{0.14}(OH)₂ precursor with a particle size of ~12 μm, the coprecipitation method was employed as

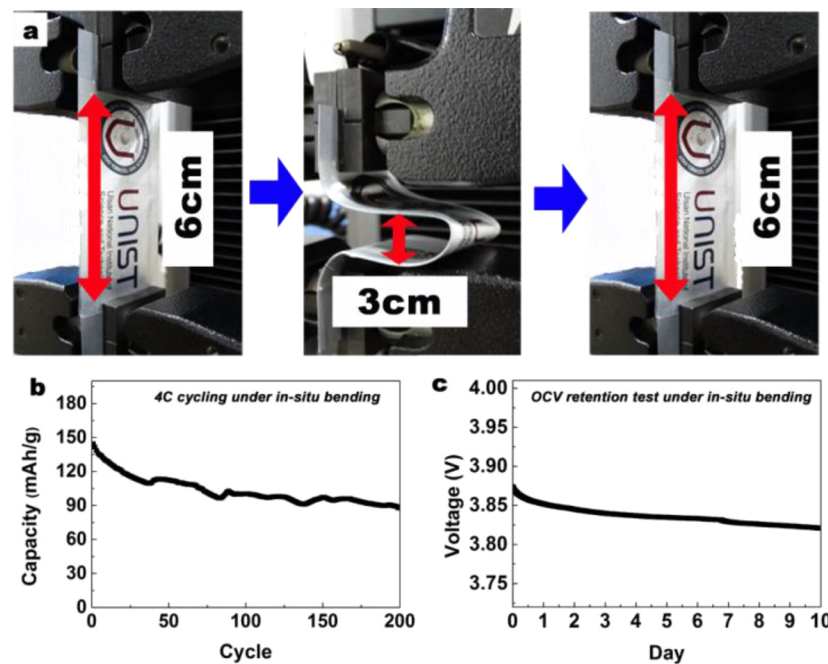


Figure 5. (a) Photographs of the pouch-type full cell before bending and after bending. (b) Plot of discharge capacity versus cycle number for the full cell at charge and discharge rates of 4 C with a bending speed of 30 mm min^{-1} under 11.0 N. (c) Plot of open-circuit voltage at 3.9 V as a function of number of days in the in situ bending test.

described in ref 33.³⁵ $\text{NiSO}_4 \cdot 6\text{H}_2\text{O}$, $\text{CoSO}_4 \cdot 7\text{H}_2\text{O}$, and $\text{MnSO}_4 \cdot 6\text{H}_2\text{O}$ were mixed with a molar ratio of $\text{Ni}/\text{Co}/\text{Mn} = 75:11:14$ and with a concentration of 2.0 M in distilled water. The mixed solution was put into a continuous stirred tank reactor (CSTR) with a capacity of 7 L under N_2 atmosphere. Simultaneously, 2.0 M solutions of NaOH and the desired amount of NH_4OH solution as a chelating agent were separately fed into the CSTR kept at 50°C and $\text{pH} = 11$. The coprecipitated powder was filtered, washed with distilled water several times, and then dried at 100°C overnight. The precursor powder was mixed with $\text{LiOH} \cdot \text{H}_2\text{O}$ (molar ratio 1:1.03) at 450°C for 5 h, followed by heating at 750°C for 18 h under flowing oxygen gas. To prepare the coated VNCM cathode, 6 g of NH_4VO_3 (ammonium metavanadate) was dissolved in ethanol for 5 h at 70°C , and 1 kg of BNCM powder was added and thoroughly mixed as the temperature increased slowly to 110°C for an hour. The mixture was mixed vigorously with BNCM at 110°C until ethanol removal. The result powders were calcined at 400°C for 3 h.

Synthesis of α -Si/EG. The α -Si/EG was synthesized using the CVD method. The expanded graphite (World Tube Co. Korea) was placed in an alumina crucible in the heating zone of a quartz tube. The tube was then evacuated to eliminate air, and SiH_4 gas was flowed at 550°C for 30 min.

Electrochemical Test for the Cathode Materials. The cathode electrode is composed of cathode material, Super P as a conductive additive, and poly(vinylidene fluoride) as a binder (80:10:10 weight ratio). Coin-type lithium cells (2016R) were assembled in an argon-filled glovebox using lithium metal as a counter electrode, microporous polyethylene as a separator, and 1.15 M LiPF_6 in ethylene carbonate/dimethyl carbonate/diethyl carbonate (3/4/3 vol %; Panax Starlyte) as the electrolyte. All electrochemical tests were performed on WBCS-3000 (WonATech Co.). The galvanostatic charge-discharge tests were conducted in a voltage range of 4.5 to 3.0 V versus Li/Li^+ . The active material loading was 7 mg cm^{-2} ,

and the electrode density and thickness were 3.1 g cm^{-3} and $23 \mu\text{m}$, respectively.

Electrochemical Test for the Anode Materials. Natural graphite was mixed with sodium carboxymethyl cellulose (MW = 90 000; Sigma-Aldrich), styrene–butadiene rubber, and an α -Si/EG in a weight ratio of 85:5:10. The active material loading was 5.3 mg cm^{-2} , and the electrode density and thickness were $\sim 1.5 \text{ g cm}^{-3}$ and $49 \mu\text{m}$, respectively. Deionized water was added to form a homogeneous slurry, which was then pasted on copper foil using a doctor blade. Coin-type lithium cells (2016R) were assembled in an argon-filled glovebox using lithium metal as a counter electrode, microporous polyethylene as a separator, and 1.15 M LiPF_6 in ethylene carbonate/diethyl carbonate (3/7 vol %; Panax Starlyte) with 10% fluoroethylene carbonate (FEC) additive as the electrolyte. All electrochemical tests were performed using a WBCS-3000 (WonATech Co.) at 24°C . The galvanostatic charge–discharge tests were conducted in a voltage range of 1.2 to 0.01 V versus Li/Li^+ . To measure the charging rate performance, the current was varied from 0.1 to 5 C rate.

Electrochemical Test for the Full Cell. Pouch-type cells were fabricated from a VNCM cathode, PNG-AES anode, microporous polyethylene as a separator, and 1.15 M LiPF_6 in ethylene carbonate/diethyl carbonate (3/7 vol %; Panax Starlyte) with 10% FEC additive as the electrolyte. The anode and cathode electrode areas were $2 \text{ cm} \times 6 \text{ cm}$. Each electrode had the same composition as the corresponding half-cell electrode. The cathode and anode electrode capacities were 1.5 and 1.7 mAh cm^{-2} , respectively. The pouch-type full cell capacity was 15.6 mAh and the N/P ratio (negative electrode capacity/positive electrode capacity) was 1.15 . The pouch-type full cells were assembled in a dry room with a H_2O level of $<100 \text{ ppm}$. All electrochemical tests were performed on a WBCS-3000 (WonATech Co.). Cycling tests were performed on the cells at 0.1 and 20 C rates under constant current (CC) mode in the voltage range between 4.3 and 3.0 V at 24°C . The

cell was charged to 4.3 V at 12 C rate in CC mode and then maintained at a constant voltage (CV) of 4.3 V for 5 min. For the rate performance, the current was varied from 0.1 to 5 C rate. The in situ bending test was performed using a bending tester (INSTRON Co.) during the cycling. After the cell was fixed to the grips of tester, it was cycled at 4 C rate with 10 bending cycles per electrochemical cycle with speed of 30 mm min⁻¹ and applied force of 11.0 N.

Characterization Methods. The crystalline phase was analyzed by powder XRD (D/MAX-2200 V, Rigaku) using Cu Ka radiation at $2\theta = 15\text{--}80^\circ$. The morphology of prepared powders was examined using scanning electron microscopy (SEM, S-4800, Hitachi). TEM sample was prepared by focused ion beam (FIB, Quanta 3D FEG, FEI). The high resolution-TEM (HR-TEM, EDS, EELS, JEM-2100F, JEOL) operating at 200 kV was used for analyzing a microstructure with an atomic scale. XPS analyses were performed with a Thermo fisher, K-Alpha spectrometer using a monochromatic Al Ka radiation of an energy beam (1486.6 eV). Spectra were recorded in the constant pass energy mode at 200.0 eV using a 100 μm diameter analysis area. For the depth profile, Ar-ion etching was used for 0–200 s.

■ ASSOCIATED CONTENT

Supporting Information

Schematic illustrations, SEM images, powder XRD patterns, HR-TEM and HAADF STEM images, Warburg impedance plots, continuous cycling results, Raman spectra, voltage profiles, charge and discharge capacities, TEM images, SAED patterns, photographs of the cathode and anode electrode, and table of lattice parameters, fwhm, pH, and ICP result of BNCM and VNCM, and video clip for in situ bending test. This material is available free of charge via the Internet at <http://pubs.acs.org>.

■ AUTHOR INFORMATION

Corresponding Authors

*E-mail: spark@unist.ac.kr (S.P.)

*E-mail: jpcho@unist.ac.kr (J.C.).

Author Contributions

†M.-H.P. and M.N. contributed equally.

Notes

The authors declare no competing financial interest.

■ ACKNOWLEDGMENTS

This research was supported by the Converging Research Center Program (2013K000210).

■ REFERENCES

- (1) Kwon, Y. H.; Woo, S. W.; Jung, H. R.; Yu, H. K.; Kim, K.; Oh, B. H.; Ahn, S.; Lee, S. Y.; Song, S. W.; Cho, J.; Shin, H. C.; Kim, J. Y. *Adv. Mater.* **2012**, *24* (38), 5192–5197.
- (2) Lee, S.-Y.; Choi, K.-H.; Choi, W.-S.; Kwon, Y. H.; Jung, H.-R.; Shin, H.-C.; Kim, J. Y. *Energy Environ. Sci.* **2013**, *6* (8), 2414–2423.
- (3) Zhou, G.; Li, F.; Cheng, H.-M. *Energy Environ. Sci.* **2014**, *7* (4), 1307–1338.
- (4) Koo, M.; Park, K.-I.; Lee, S. H.; Suh, M.; Jeon, D. Y.; Choi, J. W.; Kang, K.; Lee, K. J. *Nano Lett.* **2012**, *12* (9), 4810–4816.
- (5) Choi, M. G.; Kim, K. M.; Lee, Y.-G. *Curr. Appl. Phys.* **2010**, *10* (4), e92–e96.
- (6) Gwon, H.; Hong, J.; Kim, H.; Seo, D.-H.; Jeon, S.; Kang, K. *Energy Environ. Sci.* **2014**, *7* (2), 538–551.
- (7) Wu, Z.-S.; Zhou, G.; Yin, L.-C.; Ren, W.; Li, F.; Cheng, H.-M. *Nano Energy* **2012**, *1* (1), 107–131.
- (8) Lee, S. W.; Yabuuchi, N.; Gallant, B. M.; Chen, S.; Kim, B.-S.; Hammond, P. T.; Shao-Horn, Y. *Nat. Nanotechnol.* **2010**, *5* (7), 531–537.
- (9) Weng, Z.; Su, Y.; Wang, D.-W.; Li, F.; Du, J.; Cheng, H.-M. *Adv. Energy Mater.* **2011**, *1* (5), 917–922.
- (10) Bae, J.; Song, M. K.; Park, Y. J.; Kim, J. M.; Liu, M.; Wang, Z. L. *Angew. Chem., Int. Ed.* **2011**, *50* (7), 1683–1687.
- (11) Li, Q. W.; Li, Y.; Zhang, X. F.; Chikkannanavar, S. B.; Zhao, Y. H.; Dangelewicz, A. M.; Zheng, L. X.; Doorn, S. K.; Jia, Q. X.; Peterson, D. E.; Arendt, P. N.; Zhu, Y. T. *Adv. Mater.* **2007**, *19* (20), 3358–3363.
- (12) Li, N.; Chen, Z.; Ren, W.; Li, F.; Cheng, H.-M. *Proc. Natl. Acad. Sci. U.S.A.* **2012**, *109* (43), 17360–17365.
- (13) Ozgul, Y.-I.; Thomas, L.; Ebrahim, F.; Lorenzo, M. *Nanotechnology* **2012**, *23* (25), 255604.
- (14) Bang, B. M.; Lee, J.-I.; Kim, H.; Cho, J.; Park, S. *Adv. Energy Mater.* **2012**, *2* (7), 878–883.
- (15) Ellis, B. L.; Lee, K. T.; Nazar, L. F. *Chem. Mater.* **2010**, *22* (3), 691–714.
- (16) Jia, X.; Yan, C.; Chen, Z.; Wang, R.; Zhang, Q.; Guo, L.; Wei, F.; Lu, Y. *Chem. Commun.* **2011**, *47* (34), 9669–9671.
- (17) Kim, J.; Hong, Y.; Ryu, K. S.; Kim, M. G.; Cho, J. *Electrochem. Solid-State Lett.* **2006**, *9* (1), A19–A23.
- (18) Mijung, N.; Lee, Y.; Cho, J. *J. Electrochem. Soc.* **2006**, *153* (5), A935–A940.
- (19) Kim, Y. *J. Mater. Sci.* **2013**, *48*, 8547–8551.
- (20) Zhuanga, G. V.; Chenb, G.; Shimb, J.; Songb, X.; Rossa, P. N.; Richardson, T. J. *J. Power Sources* **2005**, *134* (2), 293.
- (21) Lee, K. T.; Jeong, S.; Cho, J. *Acc. Chem. Res.* **2012**, *46* (5), 1161–1170.
- (22) Lee, J.-W.; Park, S.-M.; Kim, H.-J. *J. Power Sources* **2009**, *188* (2), 583–587.
- (23) Choi, S.; Lee, J.-I.; Park, S. *J. Mater. Chem.* **2012**, *22* (42), 22366–22369.
- (24) Cui, L.-F.; Ruffo, R.; Chan, C. K.; Peng, H.; Cui, Y. *Nano Lett.* **2008**, *9* (1), 491–495.
- (25) Zhou, G.; Wang, D.-W.; Hou, P.-X.; Li, W.; Li, N.; Liu, C.; Li, F.; Cheng, H.-M. *J. Mater. Chem.* **2012**, *22* (34), 17942–17946.
- (26) Yoshio, M.; Brodd, R. J.; Kozawa, A. *Lithium Ion Batteries*; Springer Science: New York, 2009.
- (27) Sun, Y. K.; Myung, S. T.; Park, B. C.; Prakash, J.; Belharouak, I.; Amine, K. *Nat. Mater.* **2009**, *8* (4), 320–324.
- (28) Sun, Y. K.; Chen, Z. H.; Noh, H. J.; Lee, D. J.; Jung, H. G.; Ren, Y.; Wang, S.; Yoon, C. S.; Myung, S. T.; Amine, K. *Nat. Mater.* **2012**, *11* (11), 942–947.
- (29) Rougier, A.; Gravereau, P.; Delmas, C. *J. Electrochem. Soc.* **1996**, *143* (4), 1168–1175.
- (30) Ohzuku, T.; Ueda, A.; Nagayama, M. *J. Electrochem. Soc.* **1993**, *140* (7), 1862–1870.
- (31) Delmas, C.; Menetrier, M.; Croguennec, L.; Levasseur, S.; Peres, J. P.; Pouillerie, C.; Prado, G.; Fournes, L.; Weill, F. *Int. J. Inorg. Mater.* **1999**, *1* (1), 11–19.
- (32) Kang, B.; Ceder, G. *Nature* **2009**, *458* (7235), 190–193.
- (33) Kanga, M.; Junga, J.; Leeb, S.-Y.; Ryub, J.-W.; Kim, S. W. *Thermochim. Acta* **2014**, *576* (20), 71–74.
- (34) Nguyen, C. C.; Song, S. W. *Electrochim. Acta* **2010**, *55* (8), 3026–3033.
- (35) Noh, M.; Cho, J. *J. Electrochem. Soc.* **2013**, *160* (1), A105–A111.